



Effect of TiB_2 on the Microstructure and Mechanical Properties of $TiB_2/Al-5Cu$ Matrix Composites

JINGCHUAN TANG ^{1,2,4} MOHD ZAIDI OMAR,² RIPENG JIANG,³
and INTAN FADHLINA MOHAMED²

1.—Department of Mechanical, Electrical and Information Engineering, Changde Vocational Technical College, Changde 415000, China. 2.—Department of Mechanical and Manufacturing Engineering, Faculty of Engineering and Built Environment, Universiti Kebangsaan Malaysia, 43600 Bangi, Selangor, Malaysia. 3.—Light Alloy Research Institutes, Central South University, Changsha 410083, China. 4.—e-mail: p126473@siswa.ukm.edu.my

Particle reinforcement is a proven approach to optimize the microstructure and enhance the mechanical properties of Al matrix composites. In this work, a total of six compositions of $TiB_2/ZL205A(Al-5Cu)$ composites were fabricated by the mechanical stirring fusion casting process. The effect of TiB_2 particles on microstructure and mechanical properties of composites was explored. The experimental results indicated that the grain structure of the composite material was significantly refined, with relative refinement of 23.3%, 32.1%, 42.4%, 49.5%, and 51.6%, respectively, after the addition of TiB_2 . With the increase of TiB_2 content, TiB_2 particles can be better attached near the second phase, while agglomeration occurs easily when the content is too high. The mechanical performance results show that the 2.0 wt.% $TiB_2/Al-5Cu$ composite material has the best mechanical properties, with tensile strength (TS), yield strength (YS), and elongation (EL) of 197.8 MPa, 113 MPa, and 7.35%, respectively. Compared to Al-5Cu matrix alloy, it has increased by 51.5%, 61.4% and 129.7%, respectively. Based on the experimental results, the strengthening mechanism of Al-5Cu composites by TiB_2 particles was discussed in detail.

INTRODUCTION

Aluminum matrix composites (AMCs) are immensely popular in automotive, chemical-pharmaceutical, aerospace, and weaponry applications because of their light weight, excellent specific strength, specific stiffness, and outstanding corrosion resistance.^{1–4} Particle reinforced AMCs (PRAMCs) are usually fabricated by integrating ceramic particles as reinforcement with an Al alloy matrix.^{5,6} These composites exhibit a unique combination of the excellent specific stiffness and plasticity of metals, along with the high hardness and modulus provided by the reinforcing particles. TiB_2 reinforcement particles currently offer significant benefits due to their low density of 4.5 g/cm^3 , high modulus of

elasticity measuring 565 GPa, exceptional abrasion resistance, and cost-effectiveness.^{7–10} Therefore, it is considered as an excellent particle for reinforcing aluminum matrix composites.^{11,12}

At present, there are two main methods for introducing reinforcement particles into the matrix alloy, the external addition method and the in situ synthesis method. The in situ method offers distinct advantages over the external addition method, including a clean interface and strong interfacial adhesion.^{1,8,13} Previous studies have documented the synthesis of nanoscale TiB_2 particle-reinforced AMCs using the chemical in situ reaction method within the $Al - K_2TiF_6 - KBF_4$ system.^{14,15} Wang et al.⁷ successfully synthesized in situ $TiB_2/Al-5Cu$ composite materials through a salt metal reaction route. They found that as the TiB_2 content increased, the elastic modulus of $TiB_2/Al-5Cu$ composite materials continued to increase and established the relationship between Young's modulus

and TiB₂ content by the Tsai Halpin equation. Xiao et al.¹⁶ fabricated 2.5 wt.% TiB₂/AZ91 composite materials through chemical reactions in the Al – K₂TiF₆ – KBF₄ system. Most of the TiB₂ particles, measuring < 100 nm, were evenly distributed within the composite material, as revealed by their study. In the process of mechanism analysis, dislocation reinforcement and Orowan reinforcement play a greater role in composite materials. Xie et al.¹⁷ prepared 2 wt.% TiB₂/2195 composite materials using the synergistic technology of mechanical mixing and ultrasonic casting. Under the condition of ultrasonic vibration for 180 s, the distribution of TiB₂ particles was uniform, and the TS, YS, and EL of the composite material were increased by 115.4%, 49.8%, and 342.9%, respectively. The aforementioned studies collectively demonstrate that the incorporation of TiB₂ particles can significantly enhance the performance of metal matrix composites.¹⁵

Nonetheless, the current body of research on particle-reinforced cast Al alloy composites remains somewhat limited in scope.^{18,19} Al-5Cu, a high-strength cast Al alloy, finds extensive applications in the aerospace, military, and automotive industries.²⁰ This popularity is attributed to its exceptional comprehensive mechanical properties, which encompass high specific strength, excellent ductility, and toughness.^{21,22} While it cannot be work hardened, the strength of Al-5Cu can be enhanced through the addition of reinforcing particles, resulting in improved overall strength.^{6,23} Furthermore, prior investigations have revealed that this alloy exhibits a broad solidification range and suboptimal casting performance, leading to the formation of coarse dendritic structures and secondary structures.^{24,25} TiB₂-reinforced particles have the important role of refining the microstructure and shortening the solidification interval of the alloy. The incorporation of TiB₂ particles through in situ reaction holds the potential to enhance the properties of Al-5Cu cast Al alloy. This advancement would greatly expand the applications of Al-5Cu and offer a novel approach to improving the performance of cast Al alloys.²⁶ However, little research has been done on the effect of TiB₂ particles on Al-5Cu cast Al alloys obtained by combining in situ reaction and stir casting.

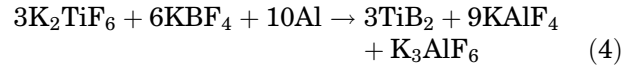
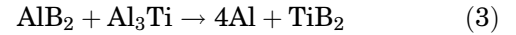
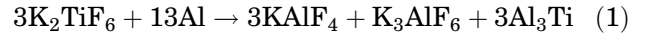
This study aims to fabricate TiB₂/Al-5Cu matrix composites with enhanced performance compared to conventional Al-5Cu while also determining the optimal weight proportion of reinforcement particles. The main innovation of this work is to introduce TiB₂ reinforcing particles to address the issue of coarse dendritic structures during the solidification process of the ZL205A alloy. Based on the ZL205 alloy, we aim to develop a novel cast aluminum alloy material that is particle-strengthened and requires no heat treatment. In the experiments, Al-5Cu matrix composites were reinforced with TiB₂ particles of different contents (0, 0.1 wt.%, 0.5 wt.%,

1.0 wt.%, 2.0 wt.%, 3.0 wt.%) through chemical reaction in the Al-K₂TiF₆-KBF₄ system at 720°C with stir casting. The effect of TiB₂ particles content on the microstructure and mechanical properties were compared detailly. The strengthening mechanism of TiB₂ particles on the AMCs has been discussed. The selection of the TiB₂ content is mainly based on the results obtained during the experimental process, proceeding step by-step. When the TiB₂ content reached 3.0 wt.%, the performance of the composite material started to decline.

EXPERIMENT

Materials

The Al-5Cu composition used in this experiment is an industry standard composition. The chemical composition of Al-5Cu was examined by direct reading spectrometer, and the results are shown in Table I. The raw materials used for in situ reaction to generate TiB₂ are K₂TiF₆, KBF₄, and Na₃AlF₆ salts²⁷ were provided by Kemiou Chemical Reagent Co., Ltd. The in situ reaction process for TiB₂ particle generation is as follows:²⁸



According to the reaction Eq. 4, apparently, the titanium and boron of TiB₂ come from K₂TiF₆ and KBF₄, respectively. Therefore, the ratio between the number of molecules for K₂TiF₆:KBF₄:TiB₂ is 1:2:1. Because the relative atomic mass of K₂TiF₆, KBF₄, TiB₂ can be derived as 240, 126, and 70, the weight ratios corresponding to this addition are 240:252:70. Therefore, when TiB₂ needs to be produced at 0.5 g, the K₂TiF₆ and KBF₄ salts are 1.7 g and 1.8 g, respectively. Table II presents the compositional distribution of mixed salts used for preparing each composite group, where Na₃AlF₆ acts as a catalyst to accelerate the reaction.²⁷

The experimental system is shown in Fig. 1, including a resistance furnace, graphite silicon carbide crucible, inert gas protection device, protection device, mechanical stirrer, and thermometer. First, approximately 500 g Al-5Cu alloy matrix material was weighed and in six batches. In Fig. 2, the dimensions of the crucible are shown. The size of the crucible is mainly selected based on the weight of the Al alloy to be cast in each instance. The weight of the aluminum alloy cast in each instance is approximately 1/3 to 1/4 of the maximum

Table I. Chemical composition of Al-5Cu alloy

Element	Cu	Ti	Mn	Zr	B	Cd	V	Fe	Si	Al
Weight/%	5.07	0.20	0.36	0.08	0.02	0.16	0.14	0.02	0.02	Bal.

Table II. In situ reaction salt mixture addition

Content of TiB ₂ (%)	0	0.1	0.5	1.0	2.0	3.0
TiB ₂ (g)	0	0.5	2.5	5	10	15
K ₂ TiF ₆ (g)	0	1.7	7.5	17	34	51
KBF ₄ (g)	0	1.8	9	18	36	54
Na ₃ AlF ₆ (g)	0	0.3	1.5	3	6	9

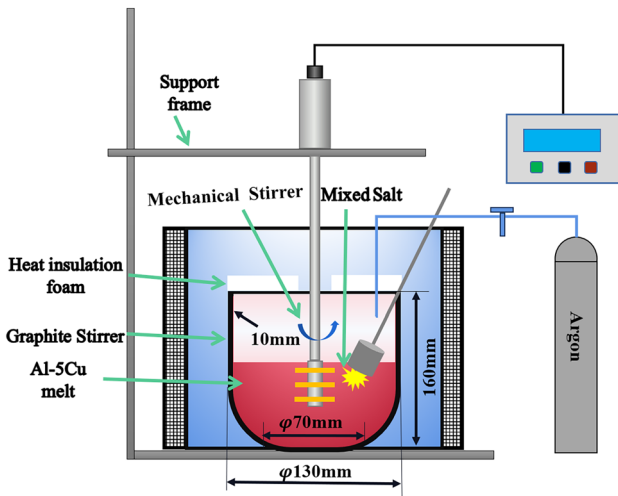


Fig. 1. Casting schematic diagram.

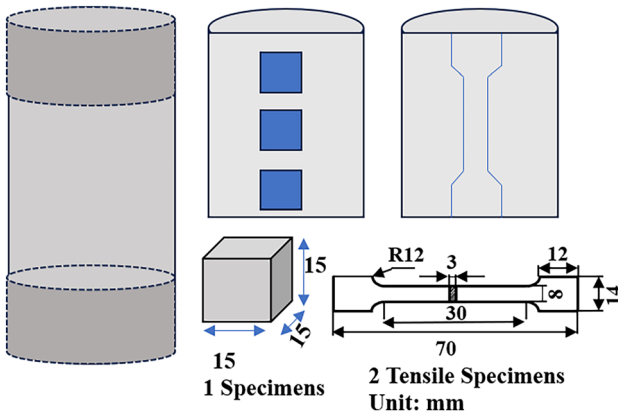


Fig. 2. Sampling schematic diagram.

capacity of the crucible. Second, according to Table II, the three reaction salts K₂TiF₆, KBF₄, and Na₃AlF₆ were weighed. Based on the amount of TiB₂ formation, 0 wt.%, 0.1 wt.%, 0.5 wt.%, 1.0 wt.%, 2.0 wt.%, and 3.0 wt.% of K₂TiF₆ and KBF₄ powders were weighed out separately. The corresponding quantity of Na₃AlF₆ powder was added to

the mixed salt powders to promote the reaction. Then, the mixed salts were ground for 30 min to achieve a uniform mixture.

The alloy was prepared by placing it in a silicon carbide graphite crucible with specific dimensions, as shown in Fig. 1, and heating it in a resistance furnace to 750 °C. After the Al-5Cu matrix alloy completely melted, degassing and slag removal were performed using inert gas. Subsequently, when the temperature of the molten Al dropped to 720 °C, a mixture of salts wrapped in Al foil was added to the melt. The weight of the aluminum foil (around 0.5 g) is insignificant and can be ignored. Mechanical stirring was carried out using a high-purity graphite impeller stirrer driven by an electric stirrer at a speed of 200 r/min for 3 min.¹⁷ Upon completion of the stirring process, any floating slag on the surface of the melt was removed, including some residual salt. Finally, the resistance furnace was turned off, and the composites was air-cooled to ambient temperature. It is cooled directly in the crucible, not cast in a mold. The varying TiB₂/ Al-5Cu content composites were prepared by adding different salt contents according to Table II.

Sampling and Testing

To characterize the microstructure and mechanical properties of the material, the sampling is shown in Fig. 2. The phase composition of the sample was determined using an x-ray diffractometer (XRD, D8 advance, Brooke, Germany). The metallographic structures of the samples were etched with a mixed etching reagent (99.5 vol% H₂O and 0.5 vol% HF). A metallographic microscope (DSX500, Japan) was used for observation. The grain size was calculated using the linear intercept method (ASTM 112-10) with IPP 6.0 software.¹⁹ The tested samples were mechanically ground and polished according to standard metallographic techniques. Use scanning electron microscopy (SEM, TESCAN M10) to observe the microstructure of the sample. EDS spectroscopy was utilized to detect the content of Cu, Ti, Fe, and other elements within different groups of specimens. The SEM specimens are subjected to abrasion and polishing according to standard sample preparation methods. An electronic universal testing machine (CMT5105GL, China) was used for ambient temperature (25 °C) tensile testing of tensile specimens at a tensile speed of 2 mm/min to obtain the TS, YS, and EL of specimens. Tensile specimens are prepared and tested according to GB/T228.1-2010. Each set of tensile experiments was repeated five times.

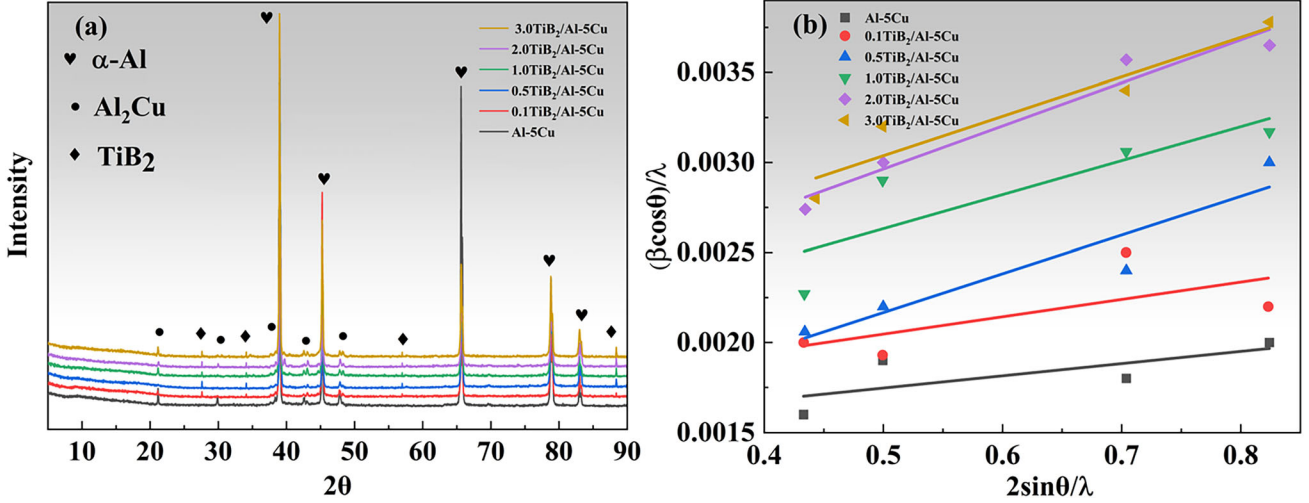


Fig 3. (a) XRD diffraction pattern, (b) Williamson-Hall plots at different processes.

EXPERIMENTAL RESULTS

Analysis of Phase Results

Figure 3 presents the XRD results, showing the emergence of a TiB₂ phase diffraction peak in the TiB₂/Al-5Cu composite material sample. This observation serves as preliminary confirmation of the TiB₂ phase presence. Furthermore, the width of the diffraction peak serves as an indicator of particle size, with a wider peak corresponding to smaller particle sizes. The intensity of the diffraction peak represents the particle content. The higher the intensity of the peak, the more particles it contains. Typically, composites have some non-equilibrium solidification during solidification. In addition, due to the difference in thermal expansion coefficients between TiB₂ particles and the Al matrix, dislocation distribution is formed within the composite. The Williamson-Hall method can be employed to calculate grain size (d), lattice distortion (e), and dislocation density (ρ) using XRD data.^{29,30} A mathematical relationship between $(\beta\cos\theta)/\lambda$ and $(2\sin\theta)/\lambda$ is assessed based on this assumption, where it is defined as:³¹

$$\frac{\beta\cos\theta}{\lambda} = \frac{1}{d} + 2e\left(\frac{2\sin\theta}{\lambda}\right) \quad (5)$$

where θ is the diffraction angle of the peak, λ (0.15406 nm) is the wavelength of the incident light source Cu Ka, and β is the half-peak width. The relationship between $\beta\cos\theta/\lambda$ and $2\sin\theta/\lambda$ is fitted according to Fig. 3a corresponding to the diffraction peaks (111), (200), (220), and (311), as shown in Fig. 3b. Accordingly, the relationship between dislocation density and lattice distortion can be calculated as follows:³²

$$\rho = \frac{2\sqrt{3}e}{db} \quad (6)$$

where ρ is dislocation density, and b is the Berg vector (0.286 nm for Al); the calculation can be finally derived from the dislocation density ρ of $5.8 \times 10^{12} \text{ m}^{-2}$, $9.1 \times 10^{12} \text{ m}^{-2}$, $1.42 \times 10^{13} \text{ m}^{-2}$, $1.93 \times 10^{13} \text{ m}^{-2}$, $2.56 \times 10^{13} \text{ m}^{-2}$, and $2.57 \times 10^{13} \text{ m}^{-2}$, respectively. This result shows that with the increase of the TiB₂ particles, the dislocation density ρ of samples is gradually increasing. This is mainly due to the difference in thermal expansion coefficient between TiB₂ particles ($4.6 \times 10^{-6}/^\circ\text{C}$) and Al matrix ($1.8 \times 10^{-5}/^\circ\text{C}$ – $2.3 \times 10^{-5}/^\circ\text{C}$), which leads to micro-deformation of grains during solidification. During the solidification process, the casting stresses are generated, which in turn introduce some dislocation lines. This will be favorable to increase the energy storage and strengthen the mechanical properties of the composites.

The α -Al Grain

The statistical results of grain size for each group of samples are presented in Fig. 4. The metallographic diagram of Al-5Cu alloy matrix material is shown in Fig. 4a. The figure illustrates a distinct coarse dendritic structure, with statistical analysis confirming a grain size of $184 \pm 11.5 \mu\text{m}$. Incorporating 0.1 wt.% TiB₂ particles through in situ reaction resulted in a refined grain size compared to Al-5Cu, transitioning the grains towards equiaxed morphology. Increasing the amount of TiB₂ particles to 1.0 wt.% led to significant refinement of the composite material particles, an increase in grain density, and a gradual evolution of grain morphology into a fine-grained state. As shown in Fig. 5, the grain size of the composites is $141 \pm 12.1 \mu\text{m}$, $125 \pm 8.5 \mu\text{m}$, $106 \pm 7.2 \mu\text{m}$, $93 \pm 5.4 \mu\text{m}$, and $89 \pm 6.8 \mu\text{m}$, respectively. Compared to the sample without adding TiB₂ particles, the refinement rates were 23.3%, 32.1%, 42.4%, 49.5%,

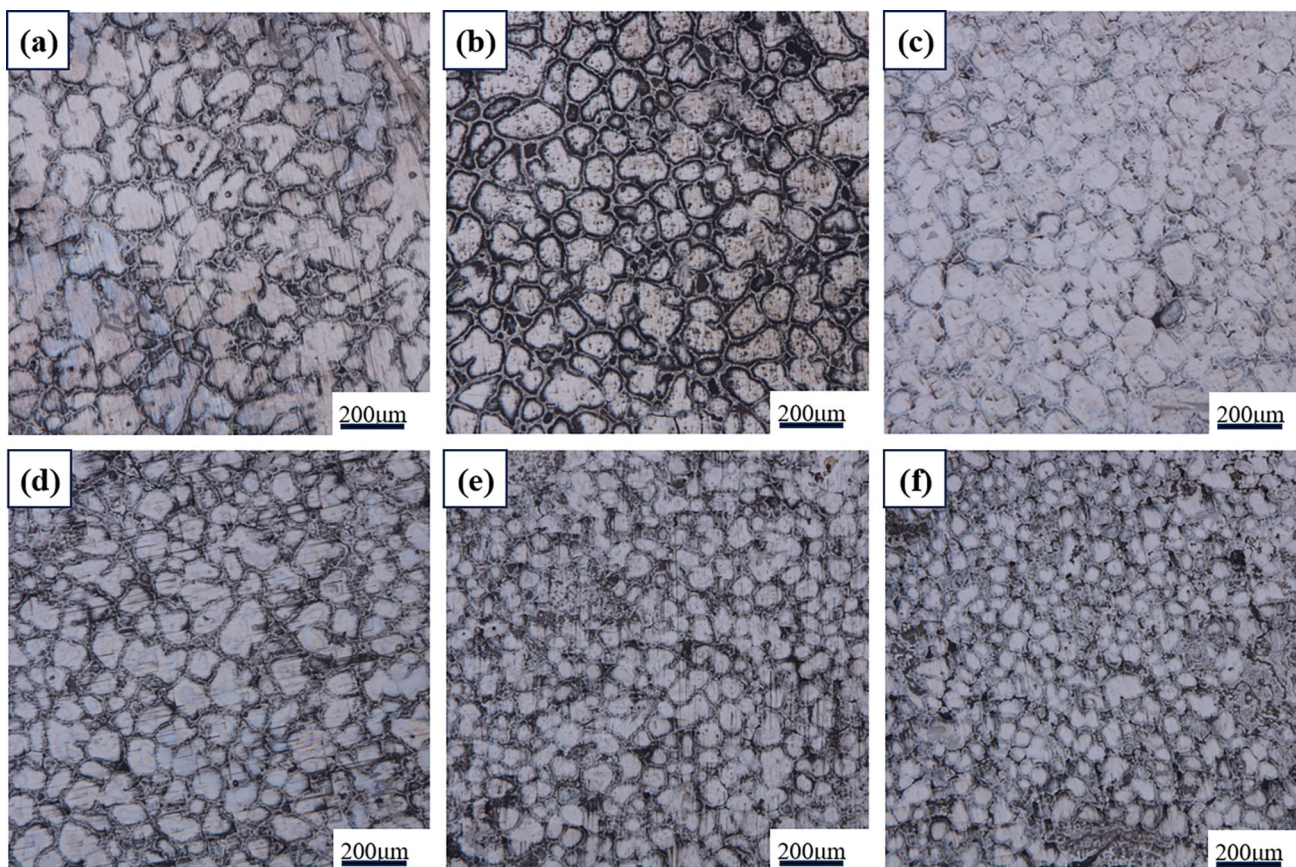


Fig. 4. Metallographic structure (a) Al-5Cu, (b) 0.1 wt.%, (c) 0.5 wt.%, (d) 1.0 wt.%, (e) 2.0 wt.%, (f) 3.0 wt. % TiB₂/Al-5Cu composites.

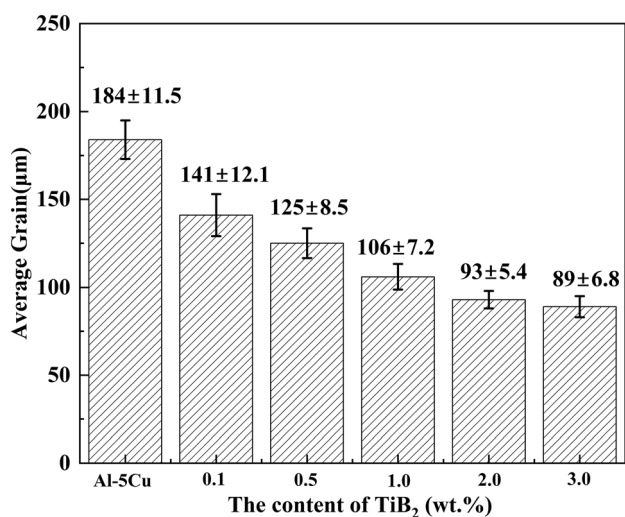


Fig. 5. Grain size of each group of specimens.

and 51.6%, respectively. Furthermore, according to the grain size tolerance results, when the TiB₂ content is 2.0 wt.%, the grain size uniformity is better.

With the increase of TiB₂ content, the degree of grain refinement gradually increased. TiB₂ as an effective nucleation site promotes the nucleation of grains inside the composite melt and inhibits the

formation of coarse dendrites. However, after TiB₂ reaches 2.0 wt.%, the grain size of TiB₂/Al-5Cu composites was reduced slightly. This indicates that an optimum value exists for TiB₂ content to produce grain refinement effect on composites. Excessive TiB₂ content does not enhance the grain refinement effect; instead, it can lead to internal agglomeration phenomena. It makes the microstructure of the composite material deteriorate.

The Second Phase

Figure 6 depicts the eutectic phase microstructure images of the composite materials of each group of samples. The microstructure of Al-5Cu alloy is shown in Fig. 6a. Figure 6b-f shows TiB₂/Al-5Cu composite materials with different contents. Figure 6 shows that as the content of TiB₂ increases, the amount of precipitation near the second phase increases. However, when the amount of TiB₂ generated reaches 3.0 wt.%, the internal porosity of the microstructure increases, which deteriorates the subsequent mechanical properties of the material. The elevated porosity levels primarily stem from the higher TiB₂ content. This is a consequence of the disparate thermal expansion coefficients between the TiB₂ particles and Al matrix, resulting in the retention of voids at the aggregation sites of TiB₂ particles during

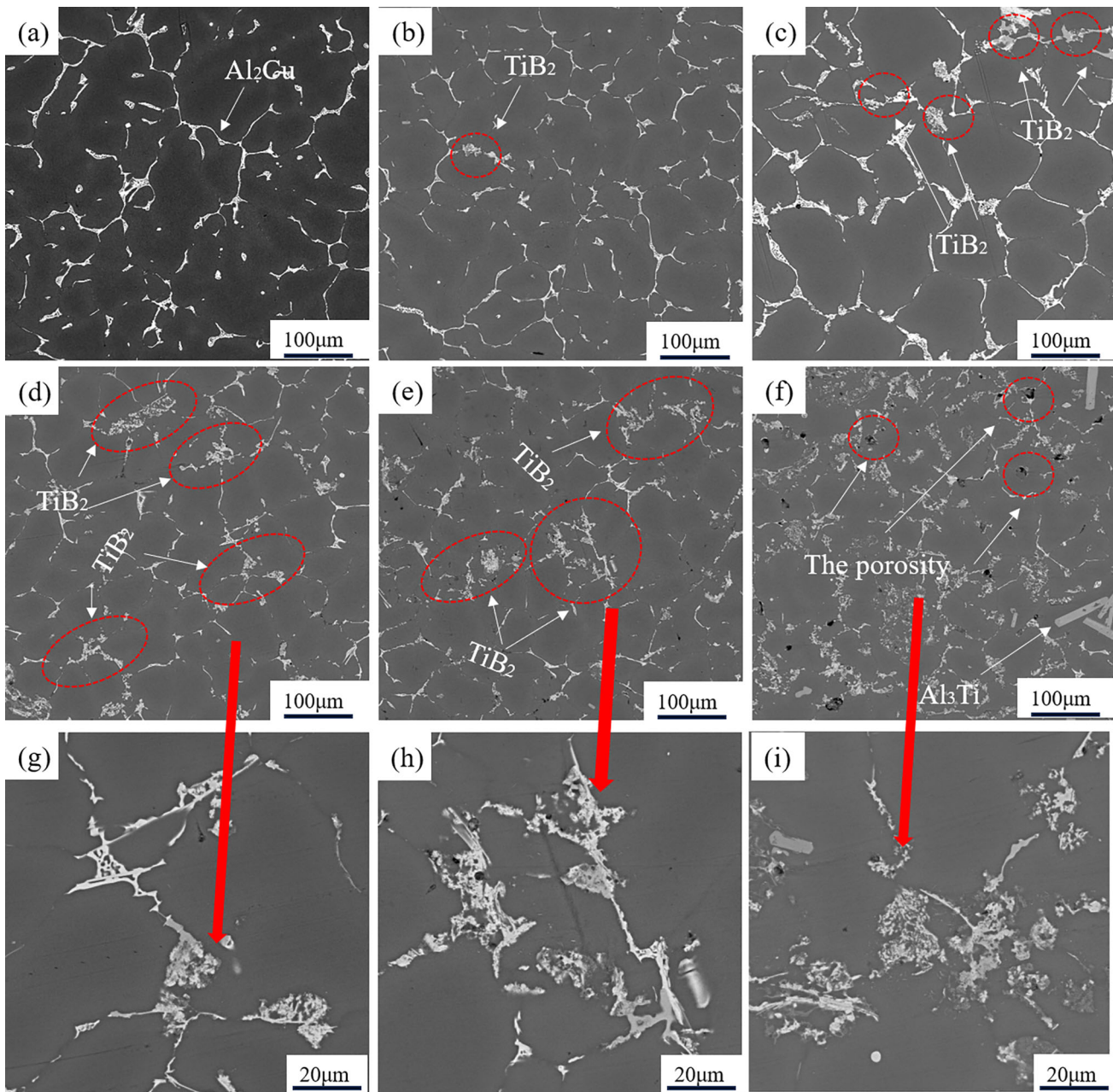


Fig 6. Eutectic phase images of (a) Al-5Cu, (b) 0.1 wt.%, (c) 0.5 wt.%, (d) 1.0 wt.%, (e) 2.0 wt.%, (f) 3.0 wt.%, enlarged area of (g-i) of TiB₂/Al-5Cu composites.

solidification. During the solidification of Al melt, voids are enveloped internally, forming voids in the solidified structure.

According to EDS and relevant literature reference results, the types of phases in Al-5Cu are α -Al, θ -Al₂Cu, θ' -Al₂Cu, and Al₃Ti, Al₃Fe. In Fig. 7, the results of the second-phase EDS inspection of the three sets of specimens are shown. Many TiB₂ particles are found in the 2.0 wt.% TiB₂/Al-5Cu and 3.0 wt.% TiB₂/Al-5Cu composites. In the 2.0 wt.% TiB₂/Al-5Cu, no large agglomeration of TiB₂ particles was observed. To further prove the Al₃Ti, Al₃Fe, and Al₂Cu intermetallic phases, EDS analysis was

performed on the secondary phases shown in Fig. 8, and the EDS results are presented in Table III. Based on the EDS results, it was further confirmed that the secondary phase shown in Fig. 8b is the Al₃Ti phase. In Fig. 8d, the dark gray phase is the Al₃Fe intermetallic, and the bright white phase is the Al₂Cu intermetallic.

However, when the TiB₂ content was increased to 3.0 wt.%, a large agglomerate region appeared, as shown in Fig. 6f and Fig. 7c. The eutectic phase of θ -Al₂Cu + Al₃Fe + TiB₂ + Al₃Fe multi-phase composite appeared in this region. This also indirectly proves that TiB₂ not only has better wettability with

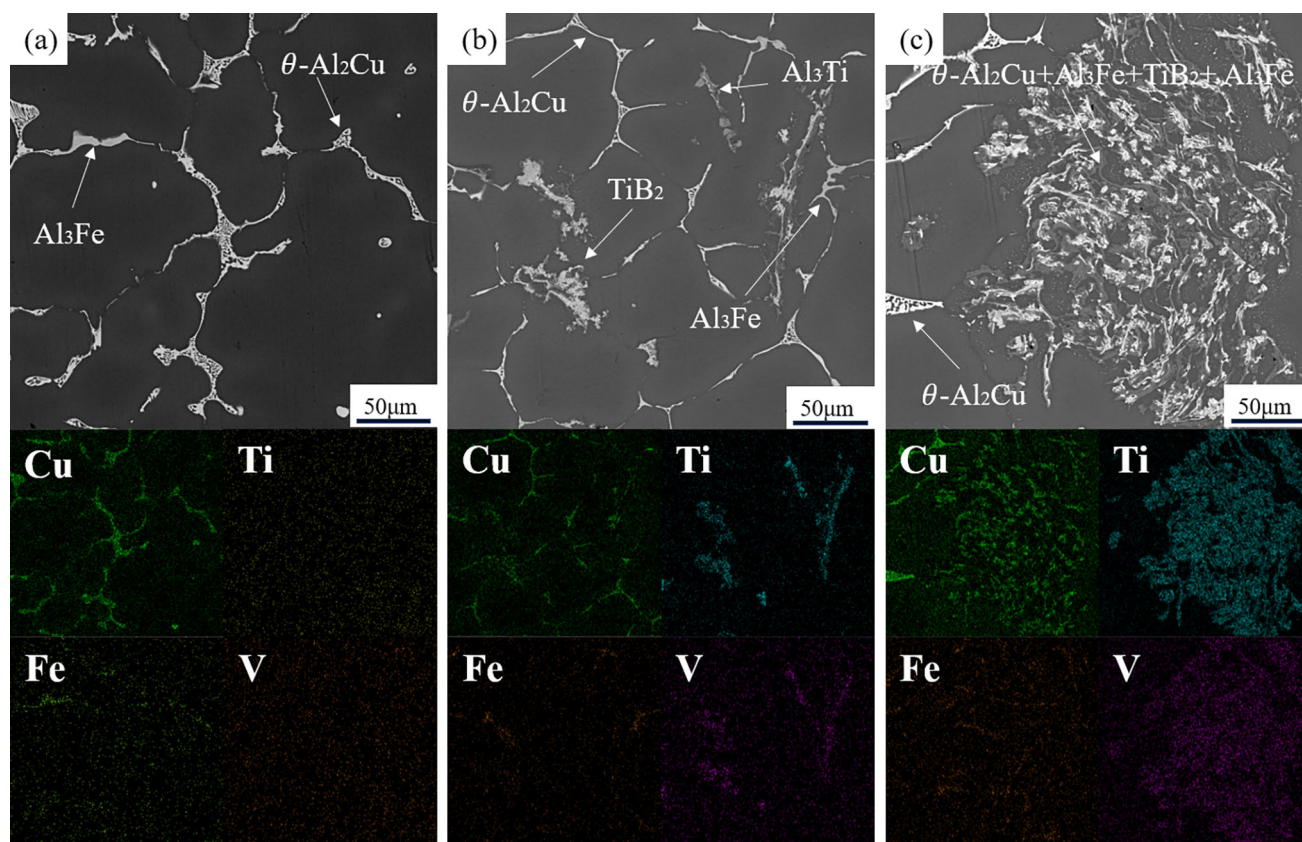


Fig. 7. EDS energy spectrum pictures of (a) Al-5Cu, (b) 2.0 wt.% TiB₂/Al-5Cu, (c) 3.0 wt.% TiB₂/Al-5Cu.

Al matrix but also with elements such as Cu and Fe, which is consistent with the study of Xie et al.¹⁷ However, this large agglomeration of multiple elements is not conducive to the improvement of material properties. It is easy to produce Fe-rich phases, Al₃Ti and other coarse eutectic phases as well as stress concentration during the deformation of the material and reduce the mechanical properties.

Mechanical Properties

The TS, YS and EL of each group of specimens are shown in Fig. 9a. The tensile strength was 130.6 MPa, 139.3 MPa, 167.5 MPa, 185.4 MPa, 197.8 MPa, and 195.3 MPa, respectively, with a relative increase of 6.7%, 28.2%, 41.9%, 51.4%, and 49.5%. After the addition of TiB₂ particles, the mechanical properties of the composite materials were significantly enhanced. Figure 9c shows the stress-strain curves for each group of specimens, which proves that the strength and elongation of the composites are increased to different degrees with the addition of TiB₂. Compared to 0 and 0.1 wt.%, the addition of 0.5 wt.%, 1.0 wt.%, and 2.0 wt.% has a significant impact on the stress-strain curve. First, the addition of the reinforcing particles enhances the heterogeneous nucleation effect, refining the grains, which significantly improves the EL of the composite material. Especially, the elongation

of the 2.0 wt.% TiB₂/Al-5Cu composite material is 7.35%, a relative increase of 129.7%. Second, TiB₂ is a high-modulus particle, and its introduction has increased the modulus of the composite material, resulting in a higher modulus exhibited by the composite material during the elastic deformation stage of the stress-strain curve. At the same time, the microhardness results in Fig. 9b show that when the hardness of the 2.0 wt.% TiB₂/Al-5Cu composite material was 90.6 HV, the relative increase was 55.7%. The change in microhardness is consistent with the change in elastic modulus exhibited in the stress-strain curve. The trend shows an initial increase followed by a decrease, which is primarily due to the severe agglomeration caused by the excessively high TiB₂ content, which is detrimental to the performance of the composite material.

The above values show that the mechanical properties of TiB₂/Al-5Cu composites did not increase continuously with the enhancement of the reinforcement particles. When the content reaches 2.0 wt.%, the tensile strength and elongation of the composites are enhanced to the relative optimum values. As shown in Fig. 7c, when the TiB₂ content is 3.0 wt.%, there is a large amount of agglomeration of TiB₂. This will easily cause stress concentration in the internal microstructure. In addition, since TiB₂ belongs to the hard reinforced particles,

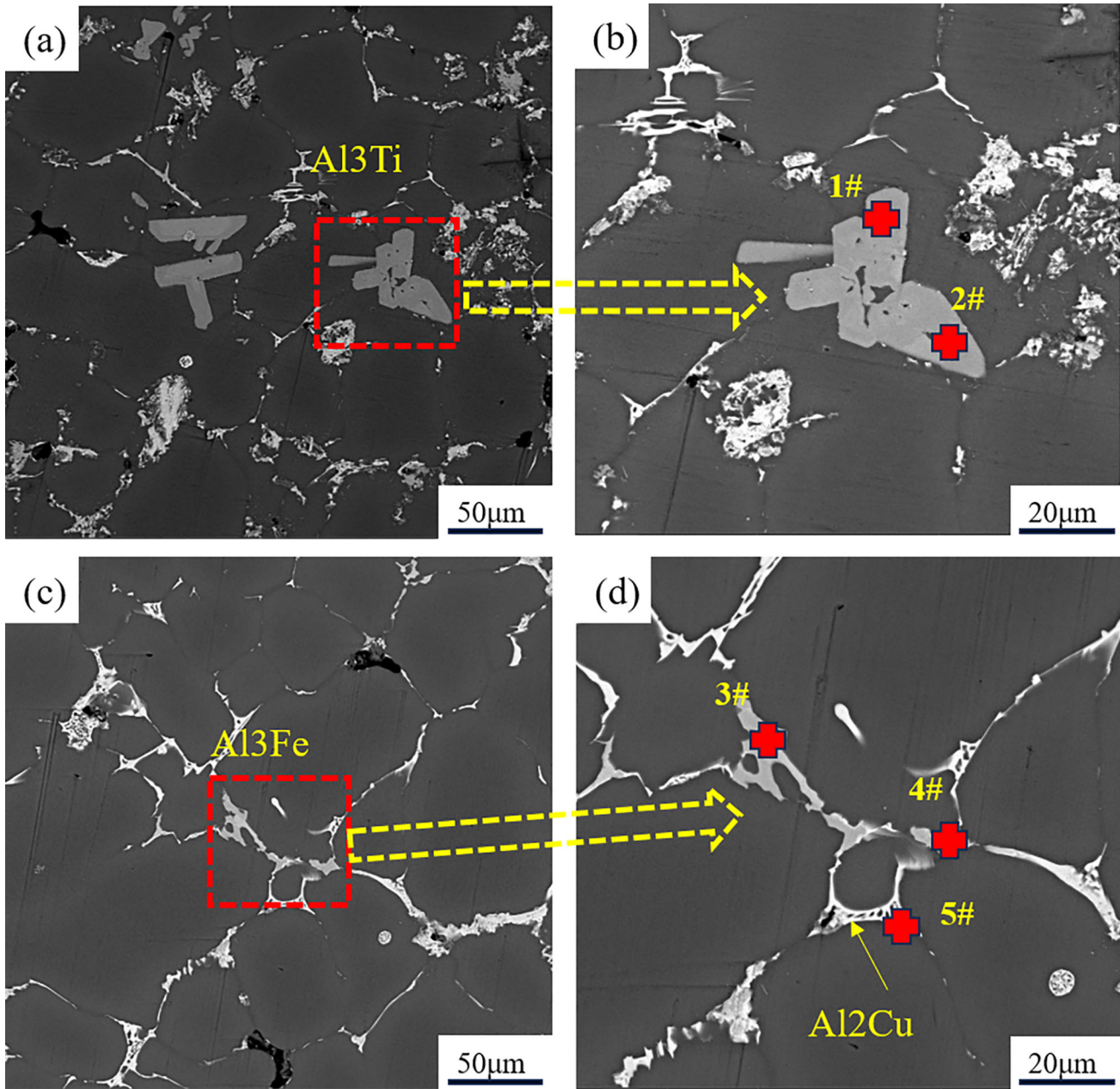


Fig. 8. (a-b) Al_3Ti second phase. (c-d) Al_3Fe and Al_2Cu second phases.

Table III. EDS energy spectrum

Position	Atomic %					
	Al	Fe	Cu	Ti	V	Others
1	72	–	–	24.4	1.3	Bal.
2	72	–	–	24.6	1.1	Bal.
3	83.9	10.3	5.8	–	–	Bal.
4	83.4	11.8	4.8	–	–	Bal.
5	79.9	–	20.1	–	–	Bal.

its modulus with is much higher than that of the matrix microstructure, and this large agglomeration will easily cause the generation of crack sources.

DISCUSSION AND ANALYSIS

Role of TiB_2 on Grain Refinement

The morphology of nanoscale TiB_2 particles under the action of TEM can be seen clearly in Fig. 10a, and the distributions of nanoscale TiB_2 particles under the action of TEM dark and bright fields are

Effect of TiB₂ on the Microstructure and Mechanical Properties of TiB₂/Al-5Cu Matrix Composites

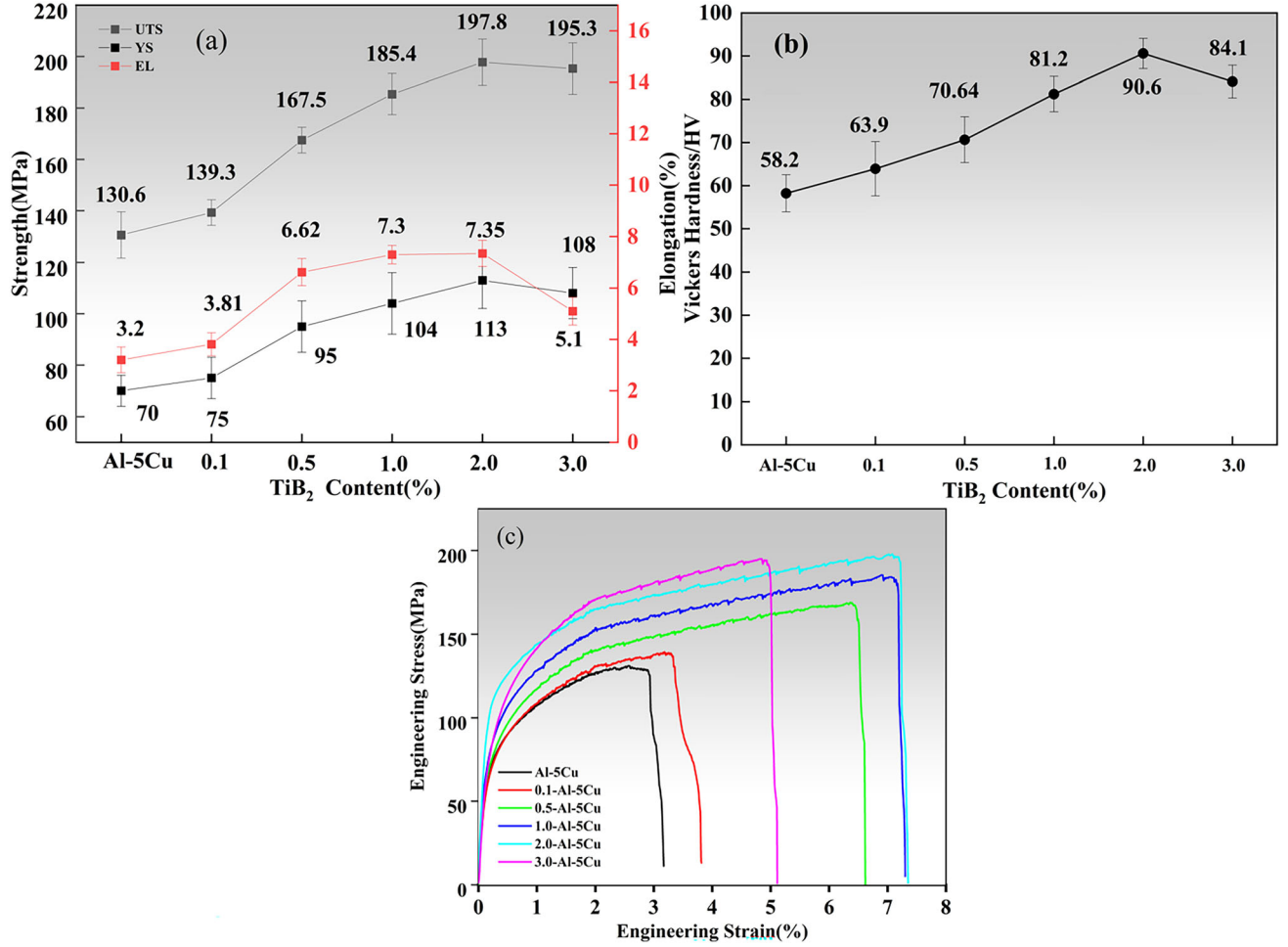


Fig. 9. Mechanical properties: (a) average value of TS, YS and EL, (b) microhardness, (c) stress-strain curve.

shown in Fig. 10b-c. Notably, the scanning area of (a) is different from those of (b-c), which are in the same area. TiB₂ particles act as the nucleus of heterogeneous nucleation and reduce the free energy of nucleation.^{33,34} According to the crystallographic matching theory, when the interplanar spacing between α -Al and TiB₂ is minimized, the interfacial energy during grain nucleation reaches its lowest value, which is highly favorable for the nucleation of α -Al grains.^{35,36} Therefore, the effective nucleation capacity of TiB₂ in the aluminum melt was assessed by calculating the atomic spacing mismatch (f_r) and the facet spacing mismatch (f_d). The calculated results provide a means to evaluate the nucleation capacity indicators of TiB₂ in Al melts. According to the E2E matching model proposed by Zhang et al., it is known that f_r and f_d are calculated as follows:³⁷

$$f_r = \frac{|r_m - r_p|}{r_p} \times 100\% \quad (7)$$

$$f_d = \frac{|d_m - d_p|}{d_p} \times 100\% \quad (8)$$

where d_m is the spacing between the matrix matched crystal planes, d_p is the spacing between the form-nucleus matched crystal planes, r_m is the spacing between the atoms in the matrix phase densely arranged direction, and r_p is the spacing between the atoms in the form-nucleus phase densely arranged direction. Typically, a good orientation relationship (OR) may exist if the a f_r is $< 10\%$. When f_d is $\leq 6\%$, the matching planes are parallel or have small rotations around the matching direction. When f_d is slightly above 6% , a good OR may still be formed by matching planes with minimal d_m mismatches.

The α -Al phase has the FCC with a crystal structure parameter of $a = 0.4041$ nm. TiB₂ is the HCP a crystal structure parameter of $a = 0.3028$ nm and $c = 0.3228$ nm.³⁷ Calculated by Eqs. 7 and 8, TiB₂ exists in two possible orientation relationships with Al as shown in Table IV. The data in the table show that Al and TiB₂ have a good orientation relationship at the matching planes $f_r = 6.1\%$ and $f_d = 0.9\%$, and the best matching plane is Al (200)[011] \parallel TiB₂(10 $\bar{1}$ 1)[1210].

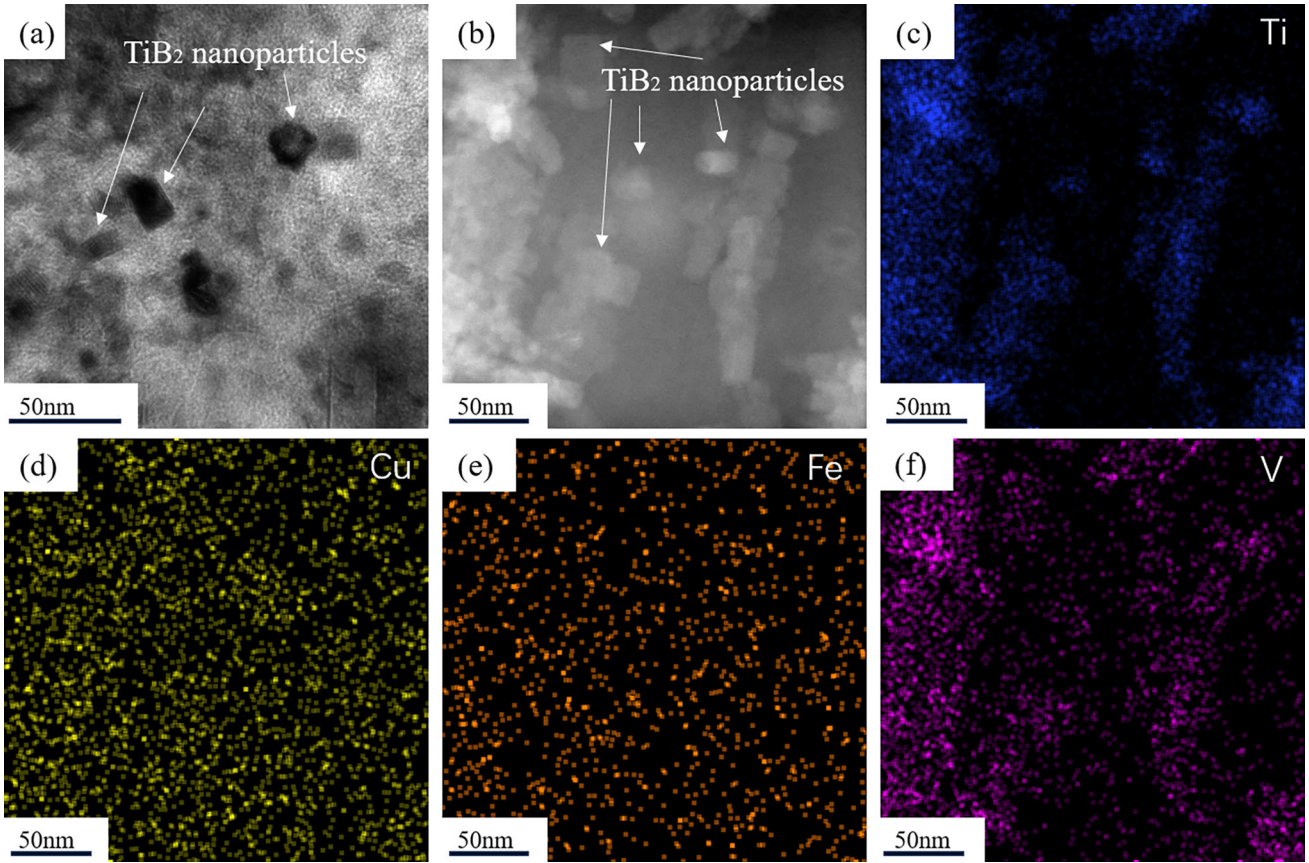


Fig. 10. The 2.0 wt.% $\text{TiB}_2/\text{Al-5Cu}$ TEM maps, (a) dark-field maps, (b) bright-field maps, EDS of (c) Ti, (d) Cu, (e) Fe, (f) V.

Table IV. The f_r and f_d between Al and TiB_2 by the E2E model

Number	$\text{TiB}_2(\text{nm})$	OR	f_r (%)	f_d (%)
1	0.3028	$\text{Al}(200)[011]//\text{TiB}_2(10\bar{1}1)[\bar{1}210]$	6.1	0.9
2	0.3228	$\text{Al}(\bar{2}20)[\bar{1}\bar{1}2]//\text{TiB}_2(11\bar{2}0)[\bar{1}\bar{1}00]$	6.1	6.1

However, it is clear from the preceding content analysis that not all TiB_2 particles will become α -Al nuclei. This phenomenon occurs because certain TiB_2 -reinforced particles become enriched at the solidification front during the solidification process, leading to a loss of the nucleation ability, as in Figs. 6f and 7c. Also, this is consistent with the results obtained from the grain size statistics. That is, the grain size fails to be further refined when the TiB_2 particles reach 2.0 wt.%. The excess TiB_2 particles will be easily agglomerated with the second phase such as Al_2Cu and Al_3Fe to form a coarse eutectic phase.

The presence of TiB_2 particles along grain boundaries (GBS) acts as grain pinning agents, effectively impeding grain boundary migration and suppressing the growth of α -Al grains. However, the presence of TiB_2 agglomerates can impede the diffusion of solute atoms such as Cu, Fe, V, etc., and promote the formation of solute element agglomerates.

Moreover, due to the favorable wettability between the Al_2Cu phase and TiB_2 particles, it tends to agglomerate and form a continuous and coarse second phase network along GBS. Consequently, the enrichment of TiB_2 particles will reduce the Cu inside the grains with severe bias at GBS.

Influence of TiB_2 on the Formation of Second Phases

From the above EDS results, the second phases in the Al-5Cu matrix are mainly θ - Al_2Cu and Al_3Fe . The size (both width and length) of the second phase in the matrix alloy is relatively large under the same preparation conditions. First, with the addition of TiB_2 particles, the effective heterogeneous nucleation density increases, and the grain refinement and equiaxial distribution will increase the grain boundary area.³⁸ This will reduce the space for the growth of second phases such as θ - Al_2Cu and Al_3Fe , which are more diffusely distributed around

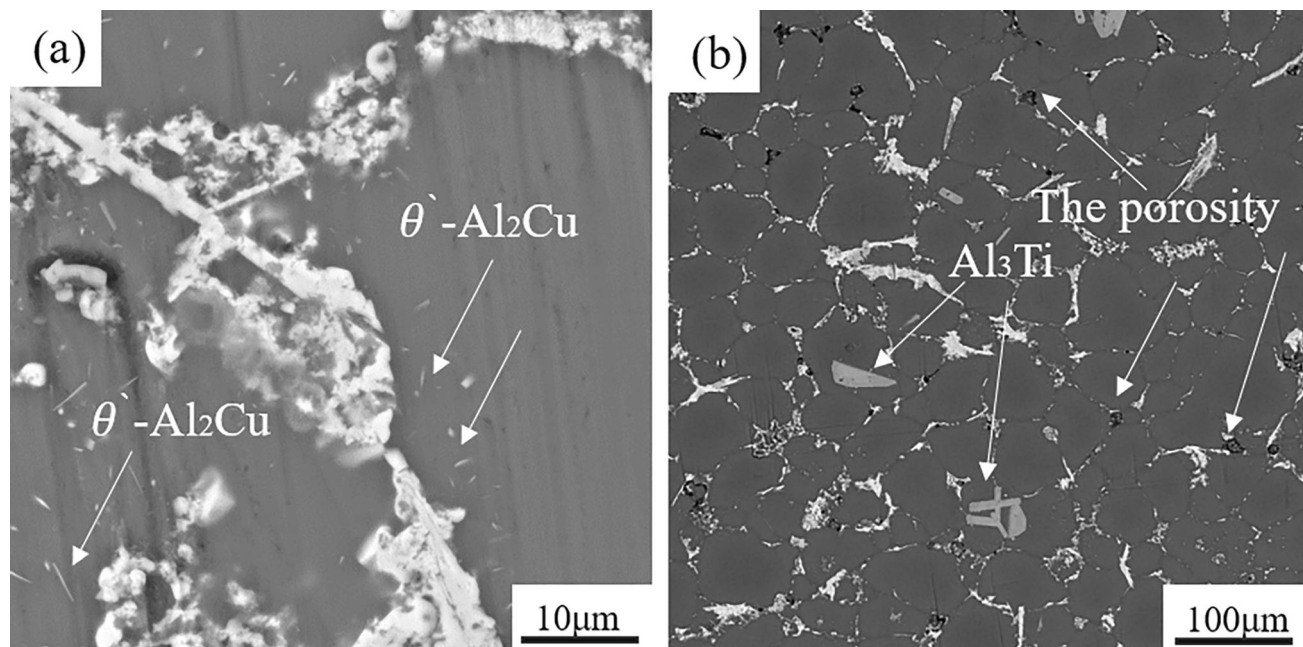


Fig. 11. SEM of (a) 2.0 wt.% $\text{TiB}_2/\text{Al-5Cu}$, (b) 3.0 wt.% $\text{TiB}_2/\text{Al-5Cu}$.

the grain boundaries and inhibit the formation of coarse eutectic phases. Second, the tiny TiB_2 particles enter into the α -Al grains, which increases the nucleation rate. Furthermore, the solid dissolution of more solute elements within the grains occurs, which results in the consumption of a portion of the solute elements. This process effectively hinders the formation of coarse eutectic phases to a certain extent. Additionally, TiB_2 particles, being high-melting-point ceramic particles, possess melting points significantly higher than those of nucleating elements such as Cu and Fe. Therefore, it can provide many nucleation sites for the formation of the second phase during the solidification process. The SEM micrograph of the 2.0 wt.% composite, as depicted in Fig. 11a, reveals the presence of a substantial number of θ - Al_2Cu phases surrounding the second phase. This phenomenon is absent in Al-5Cu alloy, indicating that the addition of TiB_2 promotes the diffuse precipitation of the second phase.

However, when the TiB_2 content is too high, many ineffective nucleation particles are present. These ineffective nucleation particles are difficult to be solidly dissolved in the Al matrix due to their high melting point. They are agglomerated together and form a coarse eutectic organization with the second phase such as θ - Al_2Cu and Al_3Fe . The significant disparity in thermal expansion coefficients between TiB_2 particles and the Al matrix can result in the formation of defects, such as shrinkage holes, within the composite material during the solidification process. These defects have a detrimental impact on the mechanical properties of the material. Moreover, when the generation content in the in situ

reaction is excessively high, there is a possibility of incomplete formation of TiB_2 particles, resulting in inadequate utilization of the Ti element. The excess Ti element will form the coarse Al_3Ti phase with the Al matrix, as shown in the Fig. 11b.

Strengthening Mechanism of Composites by TiB_2

The tensile fracture morphology of each group of specimens is shown in Fig. 12. The Al-5Cu matrix alloy presents smooth fracture traces, which belongs to the typical along-crystal fracture mode. The fracture surface shows a coarse dendritic surface consisting of large and shallow tough foci, as shown in Fig. 12a. The addition of TiB_2 enhanced the fracture pattern with the matrix. Simultaneously, the addition of TiB_2 particles leads to significant grain refinement, resulting in an increase in interfacial energy within the composite material. Consequently, the fracture mode of the composite gradually transitions from intergranular fracture to transgranular fracture mode. The more typical ones are shown in Fig. 12e, with dense distribution of tearing surfaces and tiny and deep tough nests. In the case of a TiB_2 content of 3.0 wt.%, there is a tendency for the surplus Ti element to react with the Al matrix, resulting in the formation of coarse Al_3Ti phases, as depicted in Fig. 12f. Meanwhile, with the excessive TiB_2 content, the size of the generated TiB_2 particles gradually increases as shown in Fig. 13b. This coarse second phase and TiB_2 particles reduce the interfacial energy, weaken the bond with the matrix, and are prone to generate crack sources.

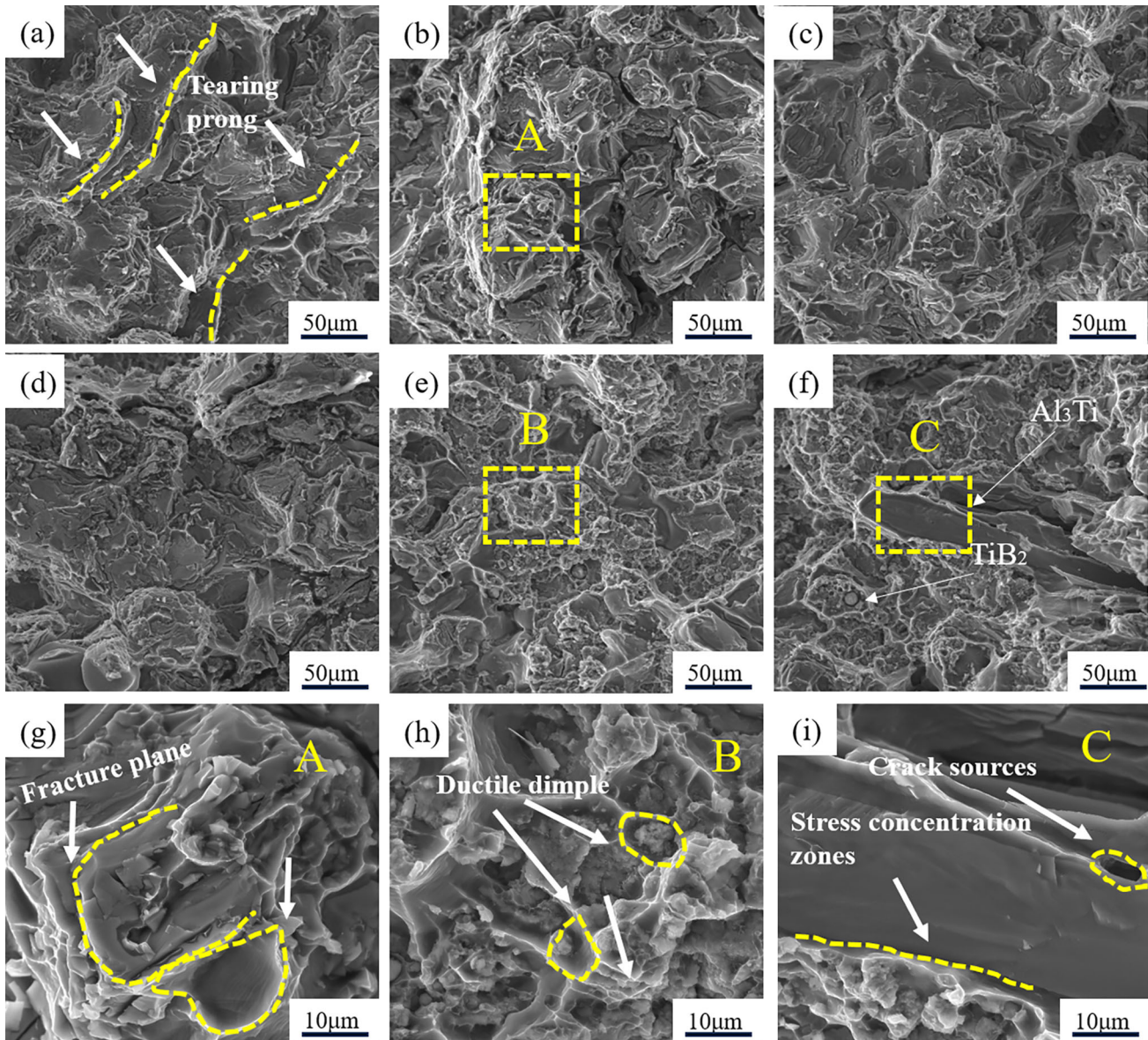


Fig. 12. Fracture morphology of (a) Al-5Cu, (b) 0.1 wt.% TiB₂/Al-5Cu, (c) 0.5 wt.% TiB₂/Al-5Cu, (d) 1.0 wt.% TiB₂/Al-5Cu, (e) 2.0 wt.% TiB₂/Al-5Cu, (f) 3.0 wt.% TiB₂/Al-5Cu, the high magnification view of (g) region A in (b), (h) region B in (e), (i) region C in (f).

To further illustrate the difference in fracture surface morphology, Fig. 12g-i shows the magnified views of regions A, B, and C, respectively. Comparison reveals that when the TiB₂ content is relatively low, the fracture surface is predominantly smooth and planar, without apparent dimple formations, further confirming the brittle fracture characteristics. When the TiB₂ content reaches 2.0 wt.%, regular dimple patterns appear on the fracture surface, as shown in (h). Figure (f) shows the local features of coarse secondary phases at the fracture surface, where stress concentration zones and crack sources are likely to form at the interface between the particles and the matrix. This is a major cause for the deterioration of mechanical properties in the 3.0 wt.% TiB₂/Al-5Cu composite material.

Figure 13a-b shows the TiB₂ particles located at the bottom of the depression within the grain, indicating their secure bonding with the matrix. This suggests that the TiB₂ particles are well incorporated within the composite. Moreover, Fig. 13c demonstrates the effect of TiB₂ pinning on the distribution of dislocations within the composite, as observed through TEM. This provides direct evidence of the reinforcing role of dislocations in the composite. When subjected to external loads, these dispersed TiB₂ particles will improve the matrix's ability to resist deformation, thus improving the mechanical properties of the material. According to the above analysis, the increase in YS of TiB₂/Al-5Cu composites is mainly attributed to the following:^{39,40} grain refinement ($\sigma_{\text{Refinement}}$), Orowan

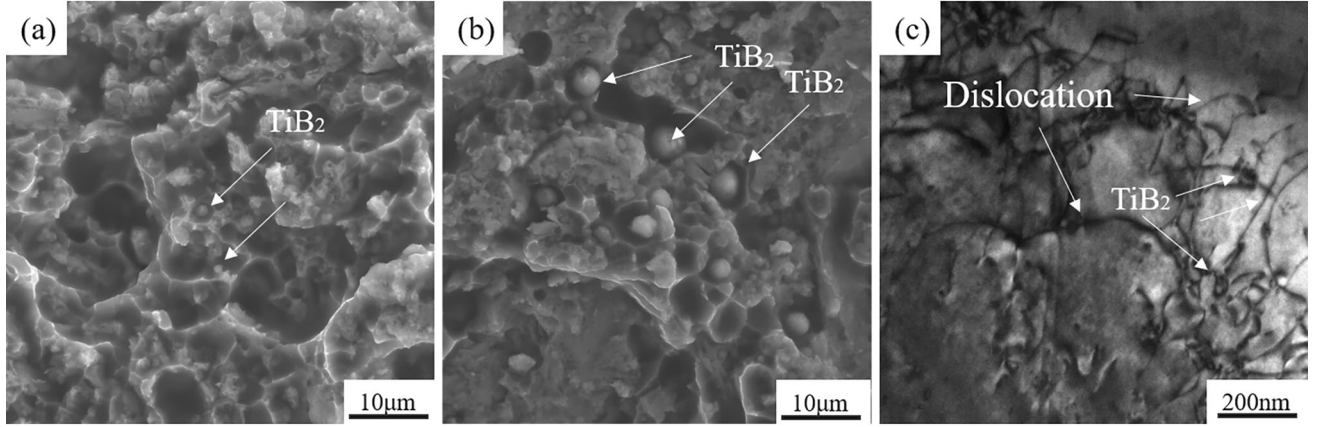


Fig. 13. Fracture topography (a) 2.0 wt.%, (b) 3.0 wt.% TiB₂/Al-5Cu, (c) dislocation of 2.0 wt.%TiB₂/Al-5Cu composites.

strengthening (σ_{Orawan}), mismatch strengthening (σ_{CTE}), and load bearing strengthening (σ_{Load}). The theoretical value of the yield strength of the composite material due to various strengthening effects can be calculated according to the following equation:⁴¹

$$\Delta\sigma = \Delta\sigma_{\text{Refinement}} + \Delta\sigma_{\text{Load}} + \left((\Delta\sigma_{\text{Orawan}})^2 + (\Delta\sigma_{\text{CTE}})^2 \right)^{1/2} \quad (9)$$

The contribution of these strengthening mechanisms to the YS of TiB₂/Al-5Cu composites is analyzed in the following section:

$$\sigma_{\text{predicted}} = \Delta\sigma + \sigma_m \quad (10)$$

The formation of TiB₂ grain content all reduces the grain size to some extent. The grain refinement increases the YS of the material, which can be calculated based on the Hall-Petch strengthening relationship, which is as follows:⁴²

$$\Delta\sigma_{\text{Refinement}} = k_{\text{HP}} \left(\frac{1}{\sqrt{d_c}} - \frac{1}{\sqrt{d_m}} \right) \quad (11)$$

where k_{HP} is the corresponding strengthening coefficient of the material (68 MPa $\mu\text{m}^{1/2}$ for Al⁴³), $d_c = 93 \mu\text{m}$ is the grain size of the 2.0 wt.% TiB₂/Al-5Cu, and $d_m = 184 \mu\text{m}$ is the grain size of the Al-5Cu alloy.

Due to the different coefficients of thermal expansion between the matrix and the reinforcing particles, certain dislocations will be easily formed during the solidification process of the composites. The enhancement of YS of composites by dislocation density is calculated as follows:⁴⁴

$$\Delta\sigma_{\text{CTE}} = \eta G_m b \sqrt{\frac{12\Delta\alpha\Delta T V_P}{bd_P(1-V_P)}} \quad (12)$$

where η is the reinforcement factor 1.25 for Al^{45,46} and $\Delta\alpha$ is the CTE difference between the matrix

and the reinforced particles. The CTE values of the Al matrix and TiB₂ particles are $25.2 \times 10^{-6}/\text{K}$ ⁴⁷ and $7.8 \times 10^{-6}/\text{K}$,⁴⁸ respectively, resulting in $\Delta\alpha = 17.4 \times 10^{-6}/\text{K}$. ΔT is the difference between the casting temperature and the test temperature.⁴⁹ The casting temperature is 1193 K, and the temperature at the end of cooling is 298 K, giving $\Delta T = 895 \text{ K}$. b is the Boolean vector 0.284, and d_P is the average size of the TiB₂ particles 800 nm. V_P is the volume fraction of reinforcing particles, converted from 2.0 to 1.5 vol%. G_m is the shear modulus of the substrate, which can be calculated by the following equation:⁵⁰

$$G_m = \frac{E_m}{2(1+\nu)} \quad (13)$$

where $E_m = 70 \text{ GPa}$ is the modulus of elasticity of the matrix, and $\nu = 0.33$ is the Poisson's ratio of the matrix.⁴⁹ Therefore, $G_m = 26.3 \text{ GPa}$ can be calculated. The calculation gives $\Delta\sigma_{\text{CTE}}$ as 26.4 MPa.

Orowan strengthening is a result of the interaction between dislocation motion and the reinforcing particles. The presence of hard TiB₂ particles poses a significant obstacle for the movement of dislocations, making it exceedingly difficult for it to pass through the particles. Instead, the dislocations undergo bending around the particles, known as Orowan bending. This mechanism restricts the movement of dislocations and contributes to the overall strengthening of the material. When encountering TiB₂ particles, as depicted in Fig. 12c, the dislocation continues to undergo bending until it eventually forms an Orowan ring around the particle. This process leads to the formation of TiB₂ particles within the matrix, creating pinning points. The presence of TiB₂ particles at grain boundaries, as illustrated in Fig. 12c, hinders the movement of neighboring dislocations, thereby enhancing the strength of the material. The contribution of Orowan strengthening to the YS of the

Table V. Contributions of different strengthening mechanism to YS of 2.0 wt.% TiB₂/Al-5Cu composites (MPa)

$\Delta\sigma_{\text{Refinement}}$	$\Delta\sigma_{\text{CTE}}$	$\Delta\sigma_{\text{Orawan}}$	$\Delta\sigma_{\text{Load}}$	$\sigma_{\text{predicted}}$	σ_{Measured}
2.0	26.4	3.6	0.42	105.2	113

composite can be calculated by the following equation:⁵⁰

$$\Delta\sigma_{\text{Orawan}} = \frac{0.13G_m b}{d_p \left[\left(\frac{1}{2V_p} \right)^{\frac{1}{3}} - 1 \right]} \ln \frac{d_p}{2b} \quad (14)$$

where G_m is the shear modulus of the matrix, b is the Burger vector, d_p is 800 nm, and V_p is the volume fraction of the reinforcing particles. $\Delta\sigma_{\text{Orawan}}$ is 3.6 MPa.

When the composite material is impacted by an external load, it helps to transfer the load to the TiB₂ particles, reducing the external load on the Al alloy matrix. This load transfer mechanism contributes to an increase in YS. This equation was used to calculate the value of the contribution of load transfer to YS can be calculated:⁵¹

$$\Delta\sigma_{\text{Load}} = 0.5V_p\sigma_m S \quad (15)$$

where σ_m is the YS of the matrix and S (close to 1) is the aspect ratio of the TiB₂ particles. $\Delta\sigma_{\text{Load}}$ is 0.42 MPa.

Table V provides the values of the contribution of the four strengthening mechanisms to the yield strength of the material as well as the theoretical values of the YS finally calculated. The σ_{Measured} deviates from the $\sigma_{\text{predicted}}$ values by 6.9% and can present good consistency. This further proves the applicability of the strengthening mechanism. According to the analysis of the fracture surface morphology, the introduction of TiB₂ particles has changed the fracture characteristics of the composite material, gradually transitioning from brittle fracture to ductile fracture. The increased number and reduced size of dimples on the fracture surface indicate that the performance of the composite material has been improved. The experimental results are consistent with the reinforcement mechanism analysis. Second, although the improvement of mechanical properties of composites and grain refinement was achieved in this work, there are still many challenges: (1) the existence of an uneven distribution of TiB₂ particle sizes and the existence of TiB₂ particles with a large size in 2.0 wt.% TiB₂/Al-5Cu composites; (2) the existence of a small range of particles agglomerated within the composites, and it is difficult to achieve a completely uniform distribution by mechanical stirring. Experimental studies will continue to address this issue in subsequent research work.

CONCLUSION

In this work, TiB₂/Al-5Cu composites were prepared by mechanical stirring melt casting process, and the evolution of the grain structure, the second phase, and the mechanical properties of each group of composites were investigated. The specific conclusions are as follows:

- (1) The crystal mismatches f_r and f_r of the TiB₂ and α -Al are 6.1%, 0.9%, respectively, with strong nucleation ability. The maximum grain refinement rate of the 2.0 wt.% TiB₂/Al-5Cu composites reached 50%.
- (2) The increase in TiB₂ particle content favors the refinement of the second phase. However, when the TiB₂ particles are excessive, it is not favorable to the performance enhancement.
- (3) TiB₂ particles play a certain role in strengthening the mechanical properties of composites. When the content of reinforcement particles is 2.0 wt.%, the TS, YS, and EL are increased by 51.5%, 61.4%, and 129.7%, respectively, compared with the Al-5Cu matrix.

ACKNOWLEDGEMENT

This work was supported by the Education Department of Hunan Province (No. 23C0478) and Universiti Kebangsaan Malaysia (UKM), Malaysia (Grant no. GP-K007539).

AUTHOR CONTRIBUTIONS

Jingchuan Tang contributed to writing-original draft and edit, funding acquisition, investigation. Mohd Zaidi Omar contributed to writing-review, editing, formal analysis and supervision. Ripeng Jiang contributed to supervision. Intan Fadhlina Mohamed contributed to supervision.

DATA AVAILABILITY

Some or all data that support the findings of this study are available from the corresponding author upon reasonable request.

CONFLICT OF INTEREST

On behalf of all the authors, the corresponding author states that there are no conflicts of interest.

REFERENCES

1. X. Zhang, Y. Chen, and J. Hu, *Progress Aerosp. Sci.* 97, 22 <https://doi.org/10.1016/j.paerosci.2018.01.001> (2018).

2. J. Xiang, L. Xie, S.A. Meguid, S. Pang, J. Yi, Y. Zhang, and R. Liang, *Comput. Mater. Sci.* 128, 359 <https://doi.org/10.1016/j.commatsci.2016.11.032> (2017).
3. H. Budiman, M.Z. Omar, A. Jalar, and J. Syarif, *Adv. Mater. Res.* 154–155, 1284 <https://doi.org/10.4028/www.scientific.net/AMR.154-155.1284> (2010).
4. H. Hashim, M.S. Salleh, M.Z. Omar, A.B. Sulong, and A.A. Rahman, *J. Tribol.* 28, 96 (2021).
5. N.K. Singh and B. Sethuraman, *Int. J. Metalcast.* 18(1), 212 <https://doi.org/10.1007/s40962-023-01009-6> (2024).
6. X.X. Huang, X. Xue, M.J. Wang, G.X. Dai, S.P. Wu, Y. Mu, and R.R. Chen, *Int. J. Metalcast.* 18(1), 759 <https://doi.org/10.1007/s40962-023-01064-z> (2024).
7. M. Wang, D. Chen, Z. Chen, Y. Wu, F. Wang, N. Ma, and H. Wang, *Mater. Sci. Eng. A* 590, 246 <https://doi.org/10.1016/j.msea.2013.10.021> (2014).
8. M. Malaki, W. Xu, A.K. Kasar, P.L. Menezes, H. Dieringa, R.S. Varma, and M. Gupta, *Metals*. 9(3), 330 <https://doi.org/10.3390/met9030330> (2019).
9. K.S. Alhawari, M.Z. Omar, M.J. Ghazali, M.S. Salleh, and M.N. Mohammed, *Procedia Eng.* 68, 186 <https://doi.org/10.1016/j.proeng.2013.12.166> (2013).
10. S.K. Gautam, M. Mallik, H. Roy, and A.K. Lohar, *Int. J. Metalcast.* 17(3), 2239 (2023).
11. A. Kumar, M. Kumar, and P.C. Verma, *Int. J. Metalcast.* 18(1), 352 <https://doi.org/10.1007/s40962-023-00988-w> (2023).
12. U. Aybarç, O. Ertuğrul, and M.Ö. Seydibeyoğlu, *Int. J. Metalcast.* 15(2), 638 <https://doi.org/10.1007/s40962-020-00490-7> (2020).
13. Y. Yang, Z. Liu, R. Jiang, R. Li, and X. Li, *J. Alloys Compd.* 811, 151991 <https://doi.org/10.1016/j.jallcom.2019.151991> (2019).
14. H. Wang, G. Li, Y. Zhao, and Z. Zhang, *J. Alloys Compd.* 509(18), 5696 <https://doi.org/10.1016/j.jallcom.2011.02.139> (2011).
15. Q. Gao, S. Wu, S. Lü, X. Xiong, R. Du, and P. An, *Mater. Sci. Eng. A* 680, 437 <https://doi.org/10.1016/j.msea.2016.10.103> (2017).
16. P. Xiao, Y. Gao, C. Yang, Z. Liu, Y. Li, and F. Xu, *Mater. Sci. Eng. A* 710, 251 <https://doi.org/10.1016/j.msea.2017.10.107> (2018).
17. Z. Xie, R. Jiang, X. Li, L. Zhang, A. Li, and Z. He, *Ultrason. Sonochem.* 90, 1 <https://doi.org/10.1016/j.ultsonch.2022.106203> (2022).
18. Y.L. Ruiying Zhang, J. Li, S. Yang, J. Sha, and Z. Shi, *Metals*. 12, 13 (2022).
19. A. Md Ali, M.Z. Omar, H. Hashim, M.S. Salleh, and I.F. Mohamed, *Rev. Adv. Mater. Sci.* 60(1), 801 <https://doi.org/10.1515/rams-2021-0062> (2021).
20. X.X. Huang, X. Xue, M.J. Wang, G.X. Dai, and S.P. Wu, *Int. J. Metalcast.* 17(4), 2970 <https://doi.org/10.1007/s40962-023-00967-1> (2023).
21. Z. Zhang, J. Liu, J. Chen, F. Wen, R. Jia, and Q. Ma, *J. Manuf. Process.* 99, 338 <https://doi.org/10.1016/j.jmapro.2023.05.040> (2023).
22. H. Liu, Z. Cai, Y. Feng, and M. Wang, *J. Mater. Res. Technol.* 26, 5321 <https://doi.org/10.1016/j.jmrt.2023.08.107> (2023).
23. T.B. Guo, B. Wang, Z.F. Zhang, Q.Z. Sun, Y.H. Jin, and W.W. Ding, *Materials* 12(10), 1688 <https://doi.org/10.3390/ma12101688> (2019).
24. B. Li, Y. Shen, and W. Hu, *Mater. Des.* 32(5), 2570 <https://doi.org/10.1016/j.matdes.2011.01.039> (2011).
25. Y. Li, G. Zhang, J. Niu, and H. Xu, *Materials* 15(20), 7087 <https://doi.org/10.3390/ma15207087> (2022).
26. H. Jiang, L. Zhang, B. Zhao, M. Sun, and M. He, *Metals* 12(12), 2037 (2022).
27. R. Pathak, P. Sanbigrahi, and R. Singh, *Mater. Sci. Eng.* 1136, 012010 (2021).
28. Y. Jia, X. Shang, YunChe, Z. Liu, Q. Liu, R. Zhang, S. Men, X. Li, and Y. Li, *Int. J. Metalcast.* <https://doi.org/10.1007/s40962-024-01316-6> (2024).
29. G.K. Williamson, W.H.H., X-ray line Broadening field Aluminum Wolfram. *Acta Mater.* 1 (1953) 259-263.
30. H. Li, P. Chen, Z. Wang, F. Zhu, R. Song, and Z. Zheng, *Mater. Sci. Eng. A* 742, 798 (2019).
31. L. Mei, X.P. Chen, G.J. Huang, and Q. Liu, *J. Alloys Compd.* 777, 259 (2019).
32. T. Liu, M.D. Vaudin, J.R. Bunn, T. Ungár, and L.N. Brewer, *Acta Mater.* 193, 115 (2020).
33. Y. Zhang, R. Li, P. Chen, Y. Yang, X. Li, and R. Jiang, *J. Alloys Compd.* 846, 156251 <https://doi.org/10.1016/j.jallcom.2020.156251> (2020).
34. B. Huang, Y. Liu, Z. Zhou, W. Cheng, and X. Liu, *Vacuum* 200, 111030 <https://doi.org/10.1016/j.vacuum.2022.111030> (2022).
35. X.P. Li, G. Ji, Z. Chen, A. Addad, Y. Wu, H.W. Wang, J. Vleugels, J. Van Humbeeck, and J.P. Kruth, *Acta Mater.* 129, 183 <https://doi.org/10.1016/j.actamat.2017.02.062> (2017).
36. H. Hashim, M.S. Salleh, and M.Z. Omar, *Rev. Adv. Mater. Sci.* 58(1), 295 <https://doi.org/10.1515/rams-2019-0035> (2019).
37. M.X. Zhang, P.M. Kelly, M.A. Easton, and J.A. Taylor, *Acta Mater.* 53(5), 1427 (2005).
38. A.P. Agrawal and S.K. Srivastava, *Int. J. Metalcast.* 18, 2545 <https://doi.org/10.1007/s40962-023-01193-5> (2023).
39. B. Zhao, Q. Yang, L. Wu, X. Li, M. Wang, and H. Wang, *Mater. Sci. Eng. A* 742, 573 <https://doi.org/10.1016/j.msea.2018.11.032> (2019).
40. Z.Y. Xu, C.F. Fang, R. Wang, C.Y. Zhong, and Y.M. Wang, *J. Alloys Compd.* 877, 160278 <https://doi.org/10.1016/j.jallcom.2021.160278> (2021).
41. S.A. Sajjadi, H.R. Ezatpour, and M. Torabi Parizi, *Mater. Des.* 34, 106 <https://doi.org/10.1016/j.matdes.2011.07.037> (2012).
42. H. Hanizam, M.S. Salleh, M.Z. Omar, A.B. Sulong, and M.A.M. Arif, *J. Alloys Compd.* 836, 155378 <https://doi.org/10.1016/j.jallcom.2020.155378> (2020).
43. A. Fadavi Boostani, S. Yazdani, R. Taherzadeh Mousavian, S. Tahamtan, R. Azari Khosroshahi, D. Wei, D. Brabazon, J.Z. Xu, X.M. Zhang, and Z.Y. Jiang, *Mater. Des.* 88, 983 <https://doi.org/10.1016/j.matdes.2015.09.063> (2015).
44. Z. Zhang and D.L. Chen, *Mater. Sci. Eng. A* 483–484, 148 <https://doi.org/10.1016/j.msea.2006.10.184> (2008).
45. L.H. Dai, Z. Ling, and Y.L. Bai, *Compos. Sci. Technol.* 61(8), 1057 (2001).
46. B.P. Sahoo, D. Das, and A.K. Chaubey, *Mater. Sci. Eng. A* 825, 141873 <https://doi.org/10.1016/j.msea.2021.141873> (2021).
47. N. Srivastava and G.P. Chaudhari, *Mater. Sci. Eng. A* 651, 241 <https://doi.org/10.1016/j.msea.2015.10.118> (2016).
48. T. Wang, Z. Chen, Y. Zheng, Y. Zhao, H. Kang, and L. Gao, *Mater. Sci. Eng. A* 605, 22 <https://doi.org/10.1016/j.msea.2014.03.021> (2014).
49. J. Liu, Z. Liu, Z. Dong, X. Cheng, Q. Zheng, J. Li, S. Zuo, Z. Huang, Y. Gao, J. Xing, and Q. Han, *J. Alloys Compd.* 765, 1008 <https://doi.org/10.1016/j.jallcom.2018.06.303> (2018).
50. Z. Zhang, and D. Chen, *Scr. Mater.* 54(7), 1321 <https://doi.org/10.1016/j.scriptamat.2005.12.017> (2006).
51. C.-S. Kim, S. Marjan, and J.B. Nezafati, *J. Mater. Sci.* 48, 4191 (2013).

Publisher's Note Springer Nature remains neutral with regard to jurisdictional claims in published maps and institutional affiliations.

Springer Nature or its licensor (e.g. a society or other partner) holds exclusive rights to this article under a publishing agreement with the author(s) or other rightsholder(s); author self-archiving of the accepted manuscript version of this article is solely governed by the terms of such publishing agreement and applicable law.